# Morphology-Controlled ZnO Nanomaterials for Enhanced Photoelectrochemical Performance

**Debabrata Pradhan[1, †], Susanta K. Mohapatra[2], Simon Tymen[1], Mano Misra[2], and Kam Tong Leung[1, *]**

[1]*WAT Lab and Department of Chemistry, University of Waterloo, Waterloo, Ontario N2L 3G1, Canada*
[2]*Department of Chemical and Metallurgical Engineering, University of Nevada, Reno, Nevada 89557, USA*

We report and compare the photoelectrochemical properties of ZnO nanowalls and nanowires electrochemically deposited on an indium-tin-oxide coated glass substrate in an aqueous zinc nitrate electrolyte at 70 °C with and without post-annealing at 400 °C. Post-annealing at 400 °C produced a drastic change in the morphology of ZnO nanowalls but not in that of ZnO nanowires. X-ray diffraction and X-ray photoelectron spectroscopy studies provide detailed characterization of the respective changes in crystallinity and composition profile of the as-deposited nanostructures before and after post-annealing. Furthermore, the optical band gap is found to be smaller for the post-annealed nanowalls and nanowires. The Mott-Schottky measurements show a negative shift in the flat-band potential for the post-annealed samples. Upon 100 mW/cm$^2$ (AM 1.5) light illumination, the photocurrent density for the as-deposited (post-annealed) nanowalls and nanowires were measured to be 0.54 mA/cm$^2$ (1.56 mA/cm$^2$) and 0.12 mA/cm$^2$ (1.03 mA/cm$^2$), respectively, at an applied potential of 0.5 V versus Ag/AgCl. The significant improvement in the photoelectrochemical properties from the post-annealed ZnO nanostructures is believed to be due to increases in crystallinity and oxygen vacancy defects, and to reduction in the band gap with the corresponding increase in light absorption at higher wavelength. This study suggests that further improvement lies in synthesizing mesoporous and/or hydrid ZnO nanostructures with semiconductor materials with a smaller band gap.

---

*Author to whom correspondence should be addressed.
Email: tong@uwaterloo.ca
†Present address: Materials Science Center, Indian Institute of Technology, Kharagpur, India.

**Keywords:** Nanostructures, Zinc Oxide, Photocatalysis, Electrodes.

## 1. INTRODUCTION

It is important to explore and develop alternative energy sources that do not produce greenhouse gases. $H_2$ is one such potential alternative fuel because it is environment-friendly and capable of efficient energy generation. Splitting of water to $H_2$ and $O_2$ in the presence of solar light using a semiconducting material as the photocatalyst therefore offers an attractive approach to harness $H_2$ energy because of the abundance of both water and sunlight. After the first demonstration of $TiO_2$ as a photocatalyst by Fujishima and Honda in the early seventy,[1, 2] several inorganic semiconductor materials (most importantly $TiO_2$, $Fe_2O_3$, $WO_3$) have been employed to split water into $H_2$ and $O_2$.[3] However, due to the pros and cons of the photocatalyst material, the big challenge in this research area remains to be the development of a robust, efficient, reliable, cost-effective, and stable semiconducting material.[4] Recent advances in nanotechnology have given the scientific community an opportunity to design and synthesize specific semiconductor nanostructures with intriguing effects on their physical and chemical properties. For example, Varghese et al.[5] and Bacsa et al.[6] have recently shown how the shape and size of $TiO_2$ and ZnO nanostructures have direct impact on the efficiency and performance of dye-sensitized solar cells, an important family of the photoelectrochemical (PEC) system. Wolcott et al.[7] and Tang et al.[8] demonstrated that PEC performance also strongly depend on the porosity and morphology of ZnO photoelectrodes and suggested the importance of controlling the materials properties for optimizing the efficiency of $H_2$ generation in the water splitting reaction.

**Article**

**Article**

Of the numerous semiconductor materials, ZnO is one of the wide-band-gap semiconductors that exhibit a high electronic mobility (205–300 and 1000 cm$^2$ V s$^{-1}$ for bulk and single nanowires, respectively), which gives rise to fast electron transport with reduced recombination loss that is highly desirable for PEC applications.[9] Furthermore, ZnO can be synthesized in various shapes with different dimensionality, including nanoparticles (0D), nanotubes, nanowires, nanorods, and nanopillars (1D), and nanodisks, nanowalls and nanobelts (2D), in a controllable size regime using either thermal evaporation or wet-chemistry techniques.[10–14] Although several studies have previously focused on the PEC properties of 1D nanostructures (such as nanowires, nanorods and nanotubes) and thin films,[15–17] little attention has been given to the 2D ZnO nanostructures. In the present work, we study the PEC properties of both 2D (nanowalls) and 1D (nanowires) ZnO nanostructures in the photocatalytic water splitting reaction. Furthermore, there are several approaches to improve the material properties in order to enhance the PEC performance in H$_2$ generation.[18–21] Annealing of the photoelectrode material is one such post-treatment that could have a significant effect on the PEC properties.[22] In particular, thermal treatment of oxide materials improves the crystallinity by reducing certain defect centers and charge recombination and by increasing the connectivity among grains (with the reduction in the grain boundaries) and therefore the photoactivity of the material. The atmospheres in which the synthesis and post-annealing of oxide materials are performed are also known to play an important role in improving the PEC performance. Synthesis of ZnO materials and annealing of TiO$_2$ nanotubes, both conducted in a nitrogen atmosphere, have been found to improve the PEC performance.[22, 23] With this in mind, we anneal the ZnO nanostructures at 400 °C in a nitrogen atmosphere and compare their PEC properties with the as-prepared nanostructures (electrodeposited at 70 °C). Our results demonstrate that the PEC performance of these ZnO nanomaterials are greatly dependent on the morphology, band gap, and crystallinity, suggesting the need for better control of the material properties in order to improve the efficiency of hydrogen generation by the water splitting reaction.

## 2. EXPERIMENTAL DETAILS

### 2.1. Electrochemical Deposition of ZnO Nanostructured Films

ZnO nanowalls and nanowires were electrodeposited on ITO-glass substrates at 70 °C in aqueous solutions of 0.1 and 0.001 M Zn(NO)$_3 \cdot$ 6H$_2$O electrolyte (mixed with a 0.1 M KCl supporting electrolyte), respectively. In brief, a three-electrode electrochemical cell was used to electrodeposit ZnO nanostructures on an ITO-glass working electrode, with Ag/AgCl and Pt wire served as the reference and counter electrodes respectively. After the deposition, electrodeposited nanostructured films were rinsed thoroughly in Millipore water and stored in a nitrogen glove box to dry for at least 24 hours prior to characterization. Some of the as-deposited samples were subsequently used for post-annealing in a nitrogen atmosphere at 400 °C for 3 h using a tube furnace.

### 2.2. Characterization of ZnO Nanomaterials

The surface morphologies of ZnO nanostructured films were examined by using a LEO FESEM 1530 field-emission scanning electron microscope, equipped with a EDAX Pegasus 1200 energy-dispersive X-ray analysis system. The crystal structures of the nanodeposits were characterized by glancing-incidence X-ray diffraction using a PANalytical X'Pert Pro MRD diffractometer with Cu K$\alpha$ radiation (1.54 Å) at an incidence angle of $\omega = 0.3°$. The surface compositions of the ZnO nanostructures were analyzed by X-ray photoelectron spectroscopy using a Thermo-VG Scientific ESCALab 250 Microprobe with a monochromatic Al K$\alpha$ source (1486.6 eV), capable of an energy resolution of 0.4–0.5 eV full width at half-maximum. The optical properties of the ZnO nanostructures were measured with a Perkin-Elmer Lambda 35 UV-vis spectrometer equipped with a Labsphere integrating sphere and a Bruker Senterra Raman spectrometer with a 532-nm diode-laser excitation source operated at 20 mW.

### 2.3. Photoelectrochemical (PEC) Hydrogen Generation from the Water Splitting Reaction

The Mott-Schottky analysis for ZnO nanostructured electrodes was carried out by conducting a standard electrochemical measurement at 3 kHz frequency in a 1 M KOH solution by scanning the potential from positive to negative direction in 50 mV/s steps. The experiments on H$_2$ generation by photoelectrolysis of water were performed in a glass cell with an anode and a cathode compartments connected by a fine porous glass frit. The photoanode in the present study was one of the ZnO nanostructured films deposited with different thicknesses on conductive ITO-glass substrates, in the form of a three-dimensional network of either interconnected nanowalls or semi-aligned nanowires, while the photocathode was a Pt foil. A reference electrode (Ag/AgCl) was also placed close to the photoanode. An electrolyte of 1 M KOH was used for the PEC measurements. The PEC cell was exposed to light through a 60 mm diameter quartz window. A computer controlled potentiostat (SI 1286, England) was employed to control the external bias and to record the photocurrent generated *in-situ* during the water-splitting reaction. A 300 W solar simulator (Model 69911, Newport-Oriel Instruments) was used to provide the AM 1.5 solar spectrum (i.e., 100 mW/cm$^2$). An UV filter (250–400 nm, Edmund Optics, U330) and a visible filter (Edmund

Optics, VG-6) were used to generate 13.9 mW/cm$^2$ of UV light and 5.27 mW/cm$^2$ of visible light on the photoanode, respectively.

## 3. RESULTS AND DISCUSSION

### 3.1. Effect of Annealing on the Morphology, Composition and Crystallinity of ZnO Nanostructures

ZnO nanowall and nanowire films were electrochemically deposited on indium-tin-oxide coated glass (ITO-glass) substrates in an aqueous electrolyte of zinc nitrate mixed with potassium chloride. The detailed deposition parameters for producing different ZnO nanostructures by electrodeposition are given elsewhere.[13] Figures 1(a and b) show the scanning electron microscopy (SEM) images of a typical nanowall film as-deposited for 1 h in an electrolyte solution of 0.1 M $Zn(NO)_3 \cdot 6H_2O$ mixed with 0.1 M KCl. The length and thickness of these nanowalls are 3–6 $\mu$m and 50–200 nm, respectively, while the nanowall surface appears to be generally smooth. These nanowalls are also found to be aligned semi-vertically on the substrate. Inset of Figure 1(a) shows cross-sectional SEM image of nanowall film, exhibiting a film thickness of 20 $\mu$m. After annealing the as-prepared nanowall film (Figs. 1(a, b)) at 400 °C for 3 h in a nitrogen atmosphere, a drastic change in the surface morphology of ZnO nanowalls (Figs. 1(c, d)) is observed. Although the 2D skeletal form remains, the post-annealed nanowalls appear to become perforated with distinct nanograins as part of the nanowall frame. Magnified SEM images (not shown) show that these nanograins are 20–30 nm diameter in size. The perforated morphology of the post-annealed ZnO nanowalls obtained in the present work could be very promising for applications in dye-sensitized solar cells because of their larger surface area available for adsorbing the dye molecules as sensitizer.[24] Figures 1(e and f) show the corresponding SEM images of a typical ZnO nanowire film as-deposited on ITO-glass for 3 h in a 0.001 M $Zn(NO)_3 \cdot 6H_2O$ mixed with 0.1 M KCl electrolyte. Measured to be 100–150 nm in diameter and 1.0–1.2 $\mu$m in length (and in film thickness), these nanowires are found to be semi-vertically oriented to the substrate (Fig. 1(e), inset). In Figures 1(f and h), we show selected regions of the nanowire films that depict horizontally placed ZnO nanowires in order to give a clearer view of the surface of the nanowires. In marked contrast to nanowalls, there is no visible change in the morphology of nanowires after annealing at 400 °C for 3 h (Figs. 1(g, h)). Further discussion regarding the formation of pores and nanoparticles in nanowalls but not nanowires upon post-annealing is given below.

Figure 2 compares the glancing-incidence X-ray diffraction (XRD) patterns of electrodeposited ZnO nanowalls and nanowires before and after annealing at 400 °C.

The more prominent XRD features of the as-deposited ZnO nanowalls are found to be in good accord with two phases corresponding to hexagonal ZnO (JCPDS file: 01-079-0207) and chlorinated zinc hydroxyl salt, i.e., $Zn_5(OH)_8Cl_2 \cdot H_2O$ (Simonkolleite) (JCPDS file: 00-007-0155). The formation of chlorinated salt during the electrodeposition of ZnO is well documented in the literature.[25] When electrodeposition is carried out in a $Zn^{2+}$ electrolyte with a concentration higher than 0.01 M, formation of chlorinated salt usually occurs. This is due to the lower value of solubility product of $Zn^{2+}$ and $Cl^-$ ions as compared to that of their ionic product. As the use of a higher electrolyte concentration (i.e., 0.1 M in the present case) is necessary for producing nanowalls, the formation of chlorinated salts in the ZnO nanowalls is therefore unavoidable. Upon annealing at 400 °C, the electrodeposited nanowalls were found to transform completely to a single phase, as evident from the only remaining prominent hexagonal ZnO diffraction pattern (Fig. 2(b)). During annealing, the chlorinated salt is converted to ZnO via the following reaction: $Zn_5(OH)_8Cl_2 \cdot H_2O(s) \rightarrow 5ZnO(s) + Cl_2(g) + 5H_2O(g)$. This process is believed to induce the formation of pores as a result of material quenching to ZnO nanoparticles inside the nanowalls as observed in the SEM images (Figs. 1(c, d)). The substantial reduction in the Cl content from 8.0–9.0 atomic% for the as-deposited nanowalls (Fig. 3(a)) to ∼2 atomic% for the post-annealed nanowalls (Fig. 3(b)) is further confirmed by the corresponding energy dispersive X-ray (EDX) analysis. The XRD patterns obtained from the as-deposited (Fig. 2(c)) and post-annealed (Fig. 2(d)) ZnO nanowires both show a most prominent diffraction feature at 34.4°, indicating the (002) growth direction of nanowires aligned perpendicular to the substrate. Weaker features attributable to $In_2O_3$ of the ITO-glass substrate evidently become more discernible in the post-annealed nanowire film (Fig. 2(d)). Because of the lower electrolyte concentration of (0.001 M) required for nanowire deposition, the solubility product of $Zn^{2+}$ and $Cl^-$ ions is higher than that of the ionic product, which does not allow the formation of chlorinated salt during the electrodeposition of nanowires. The elemental composition study by EDX (spectra not shown) further confirms the absence of chlorine in the as-deposited ZnO nanowires.

The compositions of ZnO nanostructures as-deposited and after post-annealing were further studied in detail by X-ray photoelectron spectroscopy (XPS) as a function of sputtering depth. In addition to the prominent Zn 2p and O 1s features, the survey XPS spectra (not shown) reveal a minor Cl 2p feature in the case of the nanowall samples. The presence of Cl and its role in the formation of ZnO nanowalls have been discussed in our earlier work.[13] Figures 4(a and b) show a single prominent Zn 2p$_{3/2}$ (2p$_{1/2}$) feature near 1022.7 (1045.6) eV after sputtering for over 300 s for the as-deposited and post-annealed nanowall films. The observed spin-orbit splitting of 22.90 eV is found to be in excellent accord with
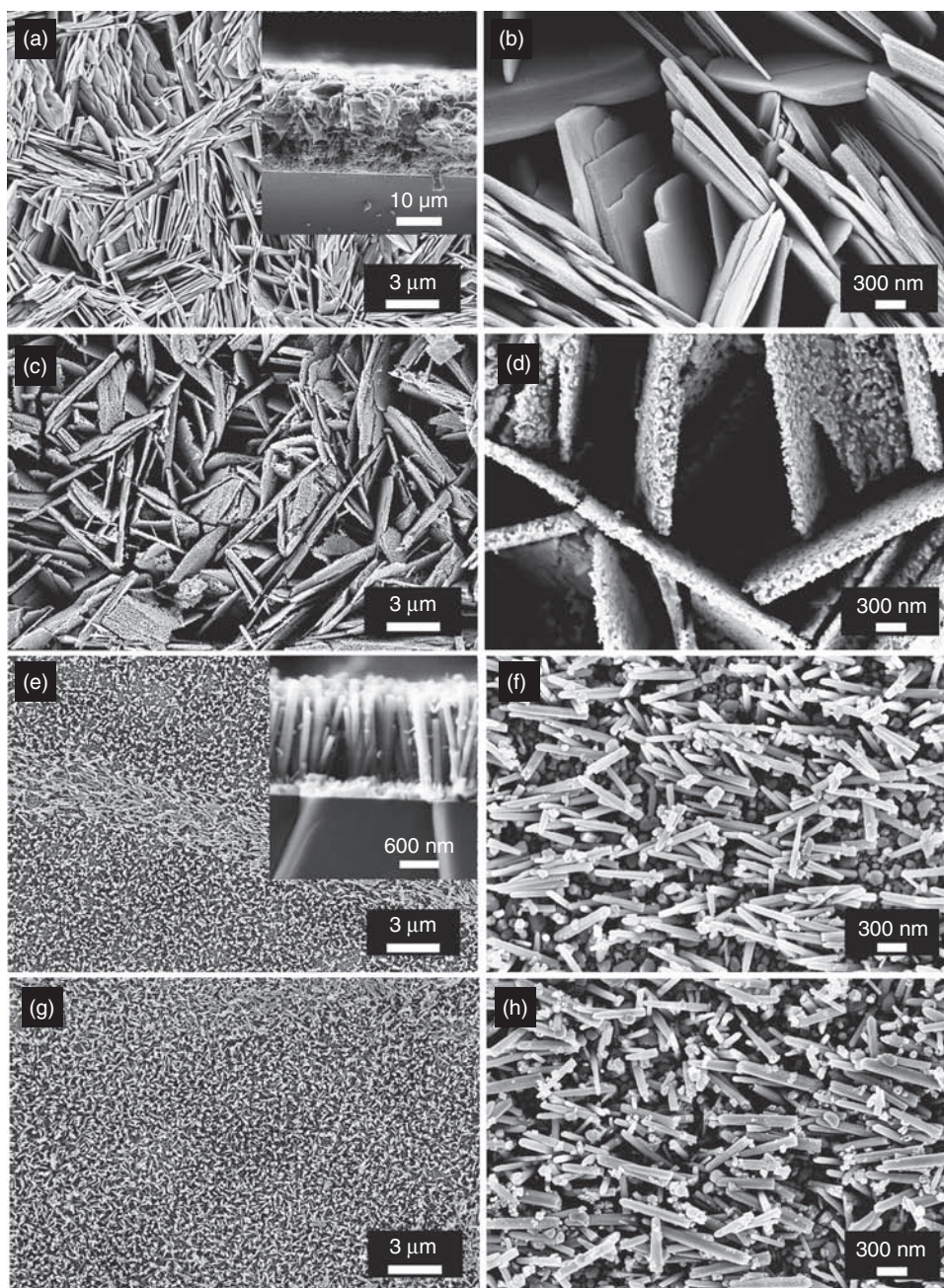
**Fig. 1.** SEM images of (a–d) ZnO nanowalls and (e–h) nanowires electrodeposited on ITO-glass substrates in respective $Zn(NO)_3 \cdot 6H_2O$ solutions of 0.1 M (for 1 h) and 0.001 M (for 3 h) (mixed with 0.1 M KCl) (a, b, e, f) at 70 °C and (c, d, g, h) post-annealed at 400 °C for 3 h.

the literature value of 22.97 eV.[26] The single Zn $2p_{3/2}$ ($2p_{1/2}$) feature clearly indicates the presence of only divalent Zn(II) oxidation state, in good correspondence to both $Zn(OH)_2$ and ZnO components. Figures 4(c and d) show the XPS spectra of the corresponding O 1s region for the as-deposited nanowalls before and after the post-annealing as a function of $Ar^+$ ion sputtering, respectively. Two O 1s components attributable to $Zn(OH)_2$ at a slightly higher binding energy and ZnO at a lower binding energy are evident. Upon sputtering for over 300 s, the O 1s features for $Zn(OH)_2$ and ZnO are found to settle at 532.8 (532.6 eV)
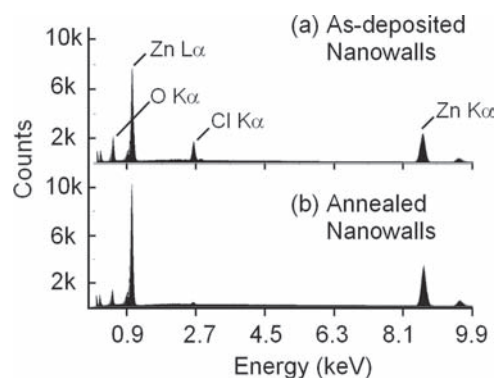
and 531.4 (531.2 eV) for the as-deposited (post-annealed) nanowalls. As $Zn(OH)_2$ is an intermediate product in the formation of ZnO nanostructures, a substantially higher concentration at the surface than the bulk is therefore expected, consistent with the depth-profiling results. The slightly higher binding energies for O 1s and Zn 2p features observed for the as-deposited nanowalls and the corresponding peak shift towards a lower binding energy upon $Ar^+$ ion sputtering are due to the removal of the non-conducting $Zn(OH)_2$ from the surface of nanowalls. In the case of the as-deposited and post-annealed ZnO
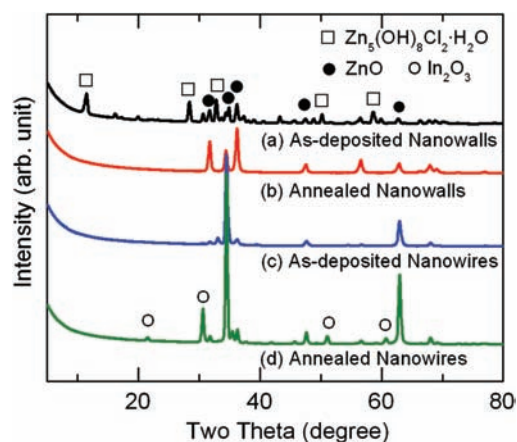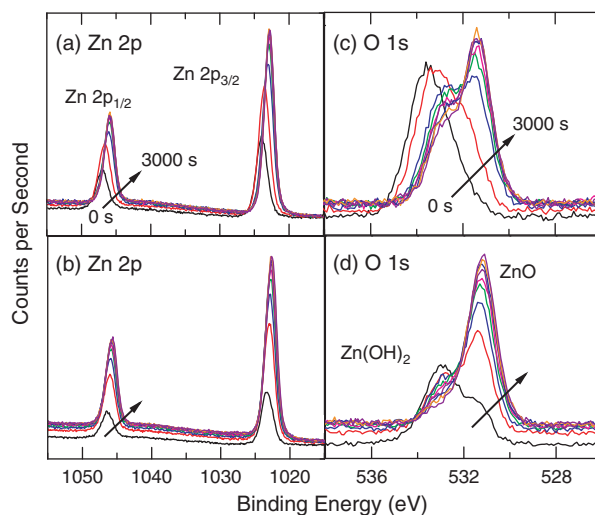
**Fig. 2.** XRD patterns of as-electrodeposited ZnO nanowalls (a) before and (b) after annealing and of ZnO nanowires (c) before and (d) after annealing, all on ITO-glass substrates. Solid circles, open squares, and open circles mark the XRD features corresponding to hexagonal ZnO (JCPDS file: 01-079-0207), chlorinated zinc hydroxyl salt, i.e., $Zn_5(OH)_8Cl_2 \cdot H_2O$ (Simonkolleite) (JCPDS file: 00-007-0155), and $In_2O_3$ of the ITO-glass substrate (JCPDS file: 01-088-2160), respectively.



**Fig. 4.** XPS spectra of (a, b) Zn 2p and (c, d) O 1s regions of ZnO nanowalls as-electrodeposited on ITO-glass substrates (a, c) before and (b, d) after annealing, and upon ion sputtering for 0, 60, 300, 600, 900, 1200, 1800, 2400 and 3000 s.

nanowires, similar XPS features (not shown) as those of ZnO nanowalls (Fig. 4) were also obtained, except with a much lower $Zn(OH)_2$ contribution and the absence of the Cl feature.

We estimate the ZnO relative concentration, in mol%, for the as-deposited and post-annealed nanowalls and nanowires by taking the ratio of the O 1s area intensity for the fitted ZnO component to the sum of the ZnO O 1s fitted area and one-half of the $Zn(OH)_2$ O 1s fitted area. The relative changes in the ZnO mol% as a function of sputtering time for the nanowall and nanowire samples are shown in Figure 5. Evidently, after sputtering for 300 s, the ZnO mol% for all the nanostructures, except for the as-deposited nanowalls, become almost constant at 85–90%. The apparent presence of a minor "residual" $Zn(OH)_2$ component beyond the surface region could be due to rapid surface hydroxylation under vacuum as proposed by Purchert et al., who observed the presence of both ZnO and $Zn(OH)_2$ *in situ* by XPS even on a ZnO
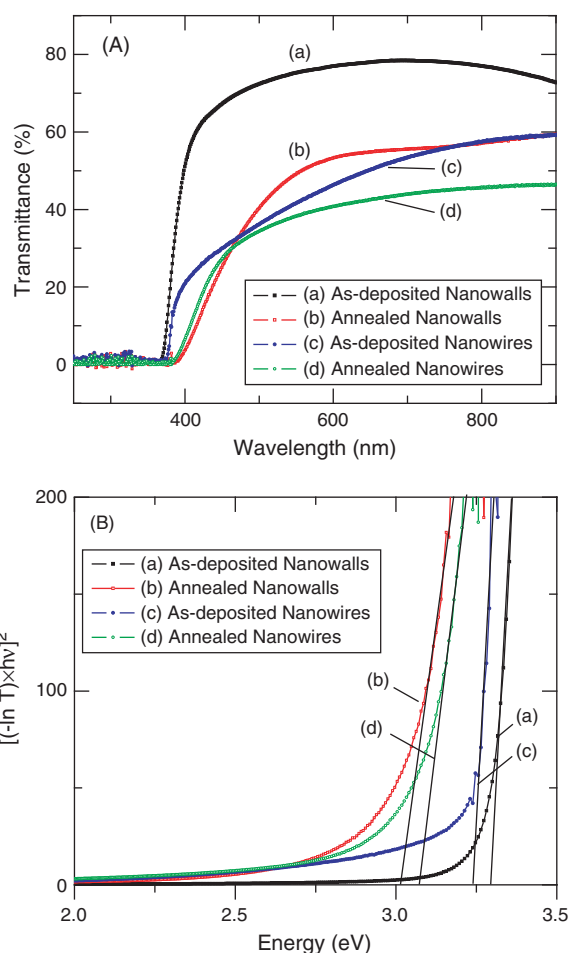
single-crystal surface freshly cleaved under vacuum.[27] The larger relative quantity of $Zn(OH)_2$ observed for the as-deposited nanowalls (20–50%) than nanowires (10–15%) can be due to the higher electrolyte concentration used in the electrodeposition, which leads to faster kinetics for $Zn(OH)_2$ formation and a larger quantity of $Zn(OH)_2$ in the bulk.[13] Upon post-annealing the nanowalls at 400 °C, there is a significant increase in ZnO mol% (and a corresponding decrease in $Zn(OH)_2$ mol%) at all sputtering depths due to the dehydration reaction of $Zn(OH)_2$ to form ZnO at a higher temperature. For the nanowires, the considerably less increase in ZnO mol% upon post-annealing reflects the lower $Zn(OH)_2$ content in the as-deposited nanowire film.



**Fig. 3.** EDX spectra of as-electrodeposited ZnO nanowalls (a) before and (b) after annealing.
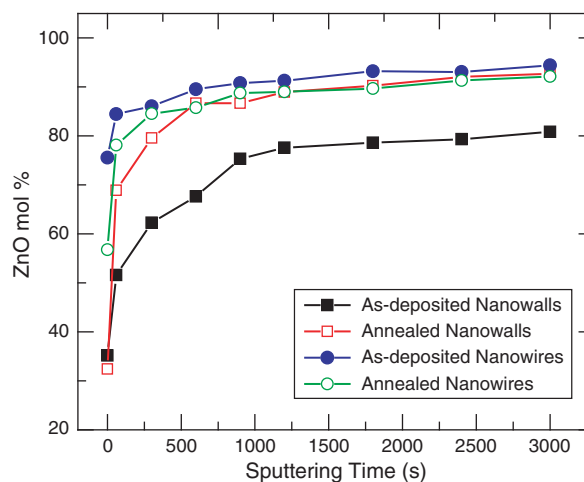
**Fig. 5.** Relative concentration (in mol%) of ZnO as a function of sputtering time for as-deposited and post-annealed ZnO nanowalls and nanowires.

**Article**

**Article**

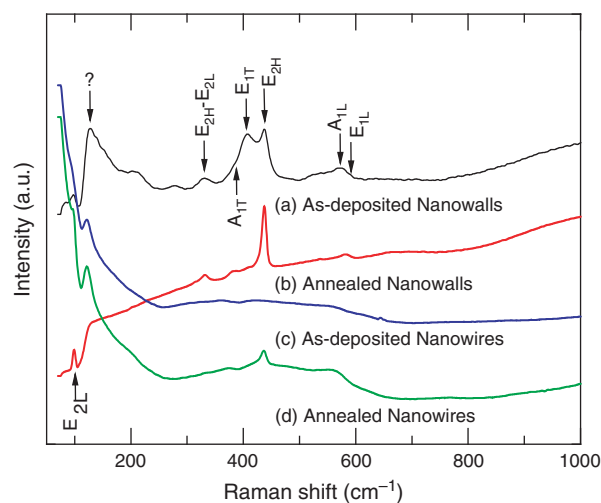### 3.2. Effect of Annealing on the Optical Properties of ZnO Nanostructures

Figure 6(A) shows the transmission spectra of as-deposited and post-annealed ZnO nanowalls and nanowires in the UV-vis range. The % transmittance (or $T$ %) is found to decrease for the post-annealed ZnO samples, depicting higher light absorption particularly in the visible region. Furthermore, the band edge appears to shift towards a higher wavelength, indicating the presence of a smaller band gap ($E_g$) for the post-annealed ZnO nanowalls and nanowires. This red-shift of band-edge wavelength and its overlapping with strong band tailing were also reported for ZnO powders synthesized at higher temperature, which was attributed to the formation of shallow levels inside the band gap as a result of the presence of impurity atoms in the lattice and/or strong disturbances of local symmetry in the ZnO lattice.[28] As ZnO is a direct band gap material, the optical band gap can be measured by extrapolating the

linear portion of the plot of $[(-\ln T) \times h\nu]^2$ versus photon energy ($h\nu$), as depicted in Figure 6(B). The band gaps of the as-deposited (post-annealed) nanowalls and nanowires are so estimated to be 3.29 eV (3.00 eV) and 3.24 eV (3.07 eV), respectively. Similar decrease in the band gap has been recently reported for ZnO films deposited at a higher temperature in a nitrogen atmosphere.[23] The observed decrease in the band gap for annealed ZnO samples in the present work could likely be attributed to either creation of oxygen vacancies or incorporation of a minute amount of N impurity (with its concentration being below the detectable limit in our EDX and XPS measurements). Dutta et al. observed a band gap shift to ~3.0 eV in the ZnO films upon annealing, which they ascribed to the formation of oxygen vacancies producing intrinsic defects.[29] These defects can have two possible consequences on the PEC performance. The electron–hole pair produced at the interface of photoelectrode and electrolyte under illumination of light can recombine at the defect centers, thereby reducing the PEC performance. On the other hand, these defects could lead to a higher light absorption in the longer wavelength region[22, 30] and may act as energy centers for the water splitting reaction favouring it in the forward direction.[31] In the present work, a larger amount of light absorption in the longer wavelength is believed to be the primary cause for the substantial increase in the PEC performance found for the post-annealed ZnO nanowalls and nanowires.

Raman spectra were taken for the as-deposited and post-annealed ZnO nanowalls and nanowires in order to further investigate their crystallinity and major structural defects. Figure 7(a) shows for the as-deposited nanowalls, two prominent low (L) and high (H) E$_2$ phonon modes: E$_{2L}$ at 99 cm$^{-1}$ and E$_{2H}$ at 437.5 cm$^{-1}$, and the corresponding weaker multi-phonon peak (E$_{2H}$–E$_{2L}$) at 332 cm$^{-1}$. We also



**Fig. 6.** (A) Transmission spectra of % transmittance (or $T$ %) versus wavelength for as-electrodeposited (a, b) ZnO nanowalls and nanowires (a, c) before and (b, d) after annealing, all on ITO-glass substrates. (B) Estimation of the corresponding band gaps from the zero-crossing values obtained by extrapolation of a linear fit to the rising edges of the respective $[(-\ln T) \times h\nu]^2$ versus photon energy ($h\nu$) plots.



**Fig. 7.** Raman spectra for as-electrodeposited (a, b) ZnO nanowalls and (c, d) nanowires (a, c) before and (b, d) after annealing, all on ITO-glass substrates.

observe the polar $A_1$ and $E_1$ modes, each of which split into transverse optical (TO) and longitudinal optical (LO) modes, with $A_1$ TO ($A_{1T}$) and $A_1$ LO ($A_{1L}$) phonon modes at ~382.0 cm$^{-1}$ and ~574.0 cm$^{-1}$, respectively, and $E_1$ TO ($E_{1T}$) and $E_1$ LO ($E_{1L}$) at 407 cm$^{-1}$ and ~581 cm$^{-1}$, respectively. These Raman phonon modes are found to be effectively at the same wavenumbers (within ±2 cm$^{-1}$) to those reported for single-crystal ZnO.[32] Upon post-annealing the nanowall film, all the TO and LO phonon peaks are greatly suppressed, while the two nonpolar $E_2$ modes ($E_{2L}$ and $E_{2H}$) have remained prominent and appear sharper (Fig. 7(b)). The suppression of TO and LO optical phonon peaks for the post-annealed nanowalls could be due to the increase in crystallinity, enhanced unidirectional crystal orientation, or/and reduction of defects related to O, interstitial Zn and free carriers.[33] Furthermore, the remaining prominent $E_{2H}$ and $E_{2L}$ modes after post-annealing are found at essentially the same locations as those for the as-deposited nanowalls, which suggest no dominant quantum confinement or other major structural defects.

The Raman spectrum from the as-deposited nanowires is broad and nearly featureless, which could be due to the rather small amount (thin film thickness) of ZnO nanowire material on the substrate (Fig. 7(c)). However, post-annealing the nanowires produces a discernible $E_{2H}$ phonon peak at 437 cm$^{-1}$ and enhanced intensity near the $A_{1L}$ and $E_{1L}$ modes at 580 cm$^{-1}$ (Fig. 7(d)). The Raman studies therefore suggest definite improvement in the structural perfection and unidirectional crystal arrangement upon post-annealing the ZnO nanowalls and nanowires, which is in good accord with our X-ray diffraction results.

### 3.3. Effect of Annealing on the Photoelectrochemical Properties of ZnO Nanostructures

The semiconductor photoelectrode properties such as donor density can be measured from the capacitance measurements.[7, 22] In order to determine the effect of post-annealing in nitrogen atmosphere on the defects and donor density of the ZnO nanostructures, Mott-Schottky analysis was performed. In particular, flat-band potential and charge carrier density can be estimated from the following Mott-Schottky relation:[7]

$$\frac{1}{C^2} = \frac{2}{q\varepsilon\varepsilon_0 N_d}\left(E - E_{FB} - \frac{kT}{q}\right) \qquad (1)$$

where $N_d$ is the donor density (i.e., electron donor concentration for an $n$-type semiconductor or hole acceptor concentration for a $p$-type semiconductor), $C$ is the capacitance of the space charge region, $\varepsilon$ is the dielectric constant of the semiconductor (8.5 for ZnO), $\varepsilon_o$ is the permittivity of free space ($8.854185 \times 10^{-12}$ F m$^{-1}$), $q$ is elementary electron charge ($1.6021 \times 10^{-19}$ C), $E$ is the applied potential, $E_{FB}$ is the flat-band potential, and $(kT)/q$ is the temperature ($T$) dependent correction term
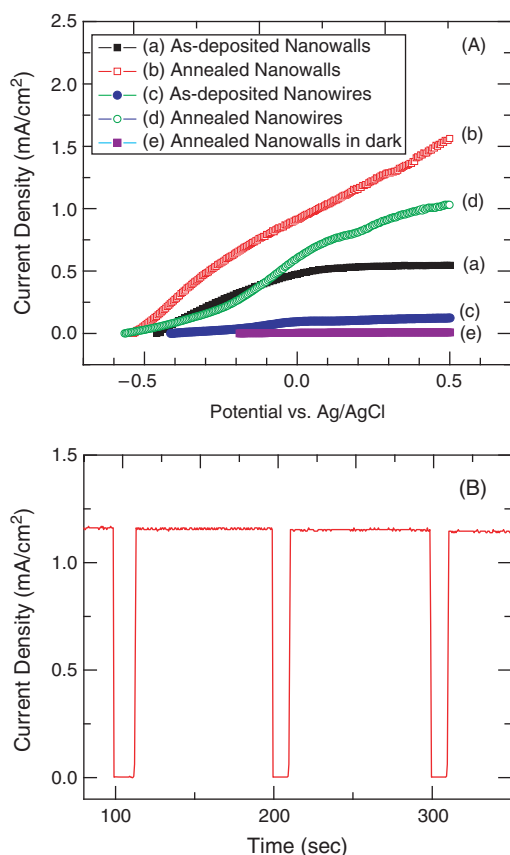
involving the Boltzmann constant $k$. By plotting $1/C^2$ versus $E$, the donor density and the flat-band potential of an $n$-type semiconductor photoanode can be obtained from the slope ($= 2/(q\varepsilon\varepsilon_o N_d)$) and intercept at $C = 0$. Figure 8 shows the $1/C^2$ versus $E$ plots for the as-deposited and post-annealed ZnO nanowalls and nanowires. The flat-band potential is found to shift from $-0.69$ V for the as-deposited nanowalls and nanowires to $-1.74$ V for the post-annealed nanowalls and $-1.0$ V for post-annealed nanowires. The shift to a more negative flat-band potential indicates that the post-annealed ZnO nanostructures are better photocatalysts than their as-deposited counterparts.[22] However, it is important to note that the unusual shift of flat-band potential to $-1.74$ V for annealed nanowalls is contrary to small change in the band gap. Further study is required to understand this unusual negative shift of flat band potential. The estimated donor densities of the post-annealed nanowalls ($6.59 \times 10^{17}$ cm$^{-3}$) and nanowires ($4.96 \times 10^{17}$ cm$^{-3}$) are found to be lower than those of as-deposited nanowalls ($3.82 \times 10^{18}$ cm$^{-3}$) and nanowires ($1.45 \times 10^{19}$ cm$^{-3}$). The lower donor densities of the post-annealed films clearly indicates that there is no N doping to the ZnO nanowalls and nanowires, which is in accord with both the EDX and XPS measurements. The lowering of the optical band gaps for the post-annealed films can therefore be attributed to defects created by oxygen vacancies.[29]

The PEC properties of as-deposited and post-annealed ZnO nanowall and nanowire electrodes were further characterized by measuring the photocurrent in a 1 M KOH electrolyte. Anodic photocurrents can be generated at the interface of a $n$-type ZnO nanostructured electrode and the electrolyte upon exposure to light (i.e., $h\nu + ZnO \rightarrow h^+ + e^-$). The photogenerated holes ($h^+$) diffuse through the semiconductor until reaching the solid/liquid interface, where they react (i.e., $2h^+ + H_2O(l) \rightarrow (1/2)O_2(g) + 2H^+$), while the photogenerated electrons are transferred
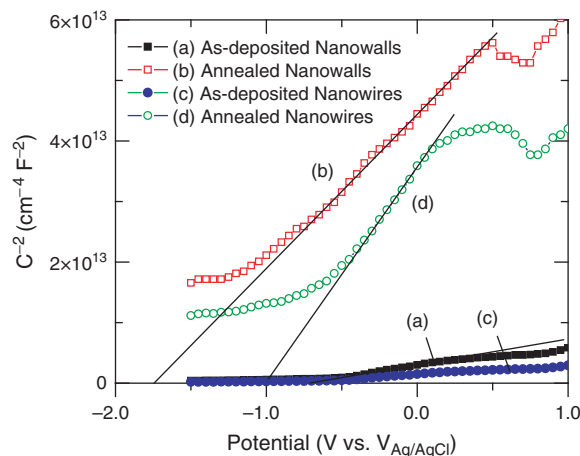


**Fig. 8.** The Mott-Schottky plot for as-electrodeposited (a, b) ZnO nanowalls and (c, d) nanowires (a, c) before and (b, d) after post-annealing, all on ITO-glass substrates.

through the external circuit to the Pt counter electrode to generate $H_2$ gas by reducing $H^+$ ions (i.e., $2H^+ + 2e^- \rightarrow H_2(g)$). Figure 9(A) shows the photocurrent generated from the ZnO nanowalls and nanowires in a 1 M KOH solution as a function of applied potential. In the absence of light illumination, the dark current density remained constant at a very low value (6.0 $\mu A/cm^2$) for the post-annealed nanowalls (Fig. 9(A-e)). The observed photocurrent in the presence of light therefore came directly from the ZnO nanostructured photoelectrodes. Moreover, we also performed separate potentiostatic current versus time measurements in the absence and presence of light to further confirm that there was no dark photocurrent contribution. The photocurrent is found to increase gradually from the open circuit condition until 0.1 V versus Ag/AgCl and then it is almost saturated for the case of as-deposited ZnO nanowalls (Fig. 9(A-a)) and nanowires (Fig. 9(A-c)). The maximum saturated photocurrent density ($J_{ph}$) obtained for the as-deposited ZnO nanowalls and nanowires are 0.54 and 0.12 mA/cm², respectively. For the post-annealed ZnO nanowalls and



nanowires, there is a near-linear increase in the photocurrent density up to 0.5 V versus Ag/AgCl. The photocurrent densities for the post-annealed ZnO nanowalls (Fig. 9(A-b)) and nanowires (Fig. 9(A-d)) at 0.5 V versus Ag/AgCl are measured to be 1.56 and 1.03 mA/cm², respectively, which are about 3 and 8 times of their respective as-deposited counterparts. The increases in current density for the post-annealed samples are also reflected by the negative shifts in the open circuit potential (or flat-band potential). Although ZnO nanowalls have higher photocurrent densities than nanowires, the nanowall film thickness ($\sim$20 $\mu m$ obtained in 1 hr of electrodeposition) was much larger than that of nanowires ($\sim$1.2 $\mu m$ obtained in 3 h of electrodeposition). Recently, Tang et al. reported a photocurrent density of 0.88 mA/cm² for urchin-line Zn/ZnO anode (prepared by a thermal vaporization process) at an applied potential of 1.0 V, which is higher than those of ZnO nanowire-array and $TiO_2$ nanotube-array anodes.[8] Wolcott et al. reported a photocurrent density of less than 200 $\mu A/cm^2$ at 1.0 V for ZnO nanostructured films obtained by pulsed laser deposition and electron beam angle deposition, while Ahn et al. obtained a photocurrent density less than 50 $\mu A/cm^2$ at 1.0 V for thin films of ZnO nanorods obtained by rf sputter-deposition.[7, 23] The measured photocurrent density in the present work is also higher than that of N and Ga co-doped ZnO films ($<$500 $\mu A/cm^2$ at 1.2 V),[34] ZnO nanocoral structures ($<$300 $\mu A/cm^2$ at 1.2 V),[35] and N-doped ZnO nanowires ($<$0.5 mA/cm² at 1.5 V).[15] The higher photocurrent density obtained from the annealed ZnO nanowalls and nanowires can be attributed to the larger surface area and the smaller band gap, thereby enabling more light absorption in the longer wavelength region. However, it is smaller than those reported recently for hybrid nanomaterials including ZnO-CdS core–shell nanowires[36] and ZnO nanowires sensitized with CdS/CdSe quantum dots.[37] In case of ZnO-CdS core–shell nanowires, Myung et al. also observed increase in the photocurrent with increasing CdS shell thickness, indicating the important role of the CdS shell (with a band gap of 2.4 eV) in enhancing the PEC performance. In the latter case, the lower band gaps of CdS and CdSe allow strong absorption in the visible spectrum up to 650 nm, thereby increasing the photocurrent density. This suggests that further improvement in the PEC performance from pristine ZnO nanowalls can be possible by synthesizing hybrid/mixed structures with lower band gap semiconductor materials.

Figure 9(B) illustrates the photocurrent density measurements as a function of time for the post-annealed ZnO nanowalls with an external bias of 0.2 V versus Ag/AgCl, with light illumination switched on and off. The rise and fall of the photocurrent density correspond satisfactorily with the photocurrent going down to zero with the light illumination on the photoanode turned off and the photocurrent returning to the original value (1.15 mA/cm²)

**Fig. 9.** (A) Photocurrent density versus applied potential under light illumination for the as-electrodeposited ZnO (a, b) nanowalls and (c, d) nanowires (a, c) before and (b, d) after annealing, all on ITO-glass substrates, under light illumination, and (e) for the post-annealed nanowall sample in the dark. (B) Time dependence of photocurrent density at an external bias of 0.2 V versus Ag/AgCl with illumination switched on and off for the post-annealed nanowalls sample.

instantly within the first second of light illumination. Unlike the previously reported case for hydrothermally prepared N-doped ZnO nanowires, in which the current density slowly decreased (from 200 to 150 $\mu$A/cm$^2$) within 180 s under illumination,[15] we observe stable and essentially constant current, i.e., at 1.15 mA/cm$^2$. This pattern of photocurrent response is highly reproducible for numerous on-off cycles of illumination, without any sign of degradation.

## 4. CONCLUSIONS

ZnO 2D (nanowalls) and 1D (nanowires) nanostructured films were electrochemically deposited on ITO-glass substrates in an aqueous solution at 70 °C and post-annealed at 400 °C in a nitrogen atmosphere, and their PEC properties for the water splitting reaction were studied in detail. The surface morphology of the electrodeposited ZnO nanowalls was found to change drastically by mild-temperature anneal, which is attributed to the conversion of chlorinated zinc hydroxyl salt to ZnO as confirmed by our XRD analysis. In contrast, no change in the surface morphology of ZnO nanowires was observed by such a post-anneal treatment, which is consistent with the absence of chlorinated zinc hydroxyl salt in their as-deposited structures. The decrease in the optical band gap for the post-annealed samples as measured from UV-vis spectroscopy is attributed to defects created by oxygen vacancies. In the PEC measurements, the post-annealed nanowall and nanowire electrodes yielded larger photocurrent densities than their as-deposited counterparts. The significant improvement in the photocurrent density for the post-annealed ZnO nanostructured photoelectrodes is attributed to increase in the surface area, improved crystallinity, a smaller band gap, and enhanced light absorption in the longer wavelength region. Furthermore, the present work also shows that the ZnO nanowall film, which can be easily electrodeposited on any conducting substrates such as glass or plastic in a short time, is a promising 2D nano-material for future photoelectrochemical devices.

## References and Notes

1. A. Fujishima, E. Sugiyama, and K. Honda, *Bull. Chem. Soc. Japan* 44, 304 (**1971**).
2. A. Fujishima and K. Honda, *Nature* 238, 37 (**1972**).
3. F. E. Osterloh, *Chem. Mater.* 20, 35 (**2008**).
4. C. A. Grimes, O. K. Varghese, S. Ranjan, and S. Light, Water, Hydrogen, the Solar Generation of Hydrogen by Water Photoelectrolysis, Springer Press, New York (**2008**).
5. O. K. Varghese, M. Paulose, and C. A. Grimes, *Nature Nanotechnology* 4, 592 (**2009**).
6. R. R. Bacsa, J. Dexpert-Ghys, M. Verelst, A. Falqui, B. Machado, W. S. Bacsa, P. Chen, S. M. Zakeeruddin, M. Graetzel, and P. Serp, *Adv. Funct. Mater.* 19, 875 (**2009**).
7. A. Wolcott, W. A. Smith, T. R. Kuykendall, Y. Zhao, and J. Z. Zhang, *Adv. Funct. Mater.* 19, 1849 (**2009**).
8. D.-M. Tang, G. Liu, F. Li, J. Tan, C. Liu, G. Q. Lu, and H.-M. Cheng, *J. Phys. Chem. C* 113, 11035 (**2009**).
9. Q. Zhang, C. S. Dandeneau, X. Zhou, and G. Cao, *Adv. Mater.* 21, 4087 (**2009**).
10. S. Kaluza, M. K. Schroter, R. N. d'Alnoncourt, T. Reinecke, and M. Muhler, *Adv. Funct. Mater.* 18, 3670 (**2008**).
11. Z. L. Wang, *Materials Today* 26 (**2004**).
12. D. Pradhan and K. T. Leung, *J. Mater. Chem.* 19, 4902 (**2009**).
13. D. Pradhan and K. T. Leung, *Langmuir* 24, 9707 (**2008**).
14. R.-Q. Song, A.-W. Xu, B. Deng, Q. Li, and G.-Y. Chen, *Adv. Funct. Mater.* 17, 296 (**2007**).
15. X. Yang, A. Wolcott, G. Wang, A. Sobo, R. C. Fitzmorris, F. Qian, J. Z. Zhang, and Y. Li, *Nano Lett.* 9, 2331 (**2009**).
16. A. I. Inamdar, S. H. Mujawar, V. Ganesan, and P. S. Patil, *Nanotechnology* 19, 325706 (**2008**).
17. W.-D. Zhang, L.-C. Jiang, and J.-S. Ye, *J. Phys. Chem. C* 113, 16247 (**2009**).
18. G. K. Mor, O. K. Varghese, R. H. T. Wilke, S. Sharma, K. Shankar, T. J. Latempa, K.-S. Choi, and C. A. Grimes, *Nano Lett.* 8, 1906 (**2008**).
19. H. E. Prakasam, K. Shankar, M. Paulose, O. K. Varghese, and C. A. Grimes, *J. Phys. Chem. C* 111, 7235 (**2007**).
20. K. Shankar, K. C. Tep, G. K. Mor, and C. A. Grimes, *J. Phys. D: Appl. Phys.* 39, 2361 (**2006**).
21. K. Shankar, G. K. Mor, H. E. Prakasam, S. Yoriya, M. Paulose, O. K. Varghese, and C. A. Grimes, *Nanotechnology* 18, 065707 (**2007**).
22. V. K. Mahajan, M. Misra, K. S. Raja, and S. K. Mohapatra, *J. Phys. D: Appl. Phys.* 41, 125307 (**2008**).
23. K.-S. Ahn, S. Shet, T. Deutsch, C.-S. Jiang, Y. Yan, M. Al-Jassim, and J. Turner, *J. Power Sources* 176, 387 (**2008**).
24. K. Nonomura, D. Komatsu, T. Yoshida, H. Minoura, and D. Schlettwein, *Phys. Chem. Chem. Phys.* 9, 1843 (**2007**).
25. S. Peulon and D. Lincot, *J. Electrochem. Soc.* 145, 864 (**1998**).
26. J. F. Moulder, W. F. Stickle, P. E. Sobol, and K. D. Bomben, Handbook of X-ray Photoelectron Spectroscopy, Chastain, J. Perkin-Elmer Corp., Eden Prairie, MN (**1992**).
27. M. K. Puchert, P. Y. Timbrell, and R. N. Lamb, *J. Vac. Sci. Technol. A* 14, 2220 (**1996**).
28. V. Ischenko, S. Polarz, D. Grote, V. Stavarache, K. Fink, and M. Driess, *Adv. Funct. Mater.* 15, 1945 (**2005**).
29. S. Dutta, S. Chattopadhyay, D. Jana, A. Banerjee, S. Manik, S. K. Pradhan, M. Sutradhar, and A. Sarkar, *J. Appl. Phys.* 100, 114328 (**2006**).
30. R. G. Breckenridge and W. R. Hosler, *Phys. Rev.* 91, 793 (**1953**).
31. J. Nowotny, T. Bak, M. K. Nowotny, and L. R. Sheppard, *Int. J. Hydrogen Energy* 32, 2630 (**2007**).
32. T. C. Damen, S. P. S. Porto, and B. Tell, *Phys. Rev.* 142, 570 (**1966**).
33. Y. W. Chen, Y. C. Liu, S. X. Lu, C. S. Xu, C. L. Shao, C. Wang, J. Y. Zhang, Y. M. Lu, D. Z. Shen, and X. W. Fan, *J. Chem. Phys.* 123, 134701 (**2005**).
34. K.-S. Ahn, Y. Yan, S. Shet, T. Deutsch, J. Turner, and M. Al-Jassim, *Appl. Phys. Lett.* 91, 231909 (**2007**).
35. K.-S. Ahn, Y. Yan, S. Shet, K. Jones, T. Deutsch, J. Turner, and M. Al-Jassim, *Appl. Phys. Lett.* 93, 163117 (**2008**).
36. Y. Myung, D. M. Jang, T. K. Sung, Y. J. Sohn, G. B. Jung, Y. J. Cho, H. S. Kim, and J. Park, *ACS Nano* 4, 3789 (**2010**).
37. G. Wang, X. Yang, F. Qian, J. Z. Zhang, and Y. Li, *Nano Lett.* 10, 1088 (**2010**).

**Article**